HHS Public Access

Author manuscript

Clin Cancer Res. Author manuscript; available in PMC 2018 January 15.

Published in final edited form as:

Clin Cancer Res. 2017 January 15; 23(2): 416–429. doi:10.1158/1078-0432.CCR-15-2134.

Evaluating acetate metabolism for imaging and targeting in multiple myeloma

Francesca Fontana[1], **Xia Ge**[2], **Xinming Su**[1], **Deep Hathi**[2], **Jingyu Xiang**[1], **Simone Cenci**[3], **Roberto Civitelli**[4], **Kooresh I. Shoghi**[2], **Walter J. Akers**[2], **Andre D'avignon**[5], **Katherine N. Weilbaecher**[1], and **Monica Shokeen**[2]

[1]Department of Medicine, Division of Molecular Oncology, Washington University School of Medicine, St. Louis, Missouri, 63110

[2]Department of Radiology, Mallinckrodt Institute of Radiology, Washington University School of Medicine, St. Louis, Missouri, 63110

[3]San Raffaele Scientific Institute (SRSI), Division of Genetics and Cell Biology, and Università Vita-Salute San Raffaele, Milano, Italy

[4]Department of Medicine, Division of Bone and Mineral Diseases, Washington University School of Medicine, St. Louis, Missouri, 63110

[5]Department of Chemistry, Washington University, St Louis 63130

Abstract

Purpose—We hypothesized that in multiple myeloma cells (MMC), high membrane biosynthesis will induce acetate uptake *in vitro* and *in vivo*. Here, we studied acetate metabolism and targeting in MMC *in vitro* and tested the efficacy of ^{11}C-acetate-PET (positron emission tomography) to detect and quantitatively image myeloma treatment response *in vivo*.

Experimental design—Acetate fate tracking using ^{13}C-edited-^{1}H NMR (nuclear magnetic resonance) was performed to study *in vitro* acetate uptake and metabolism in MMC. Effects of pharmacological modulation of acetate transport or acetate incorporation into lipids on MMC cell survival and viability were assessed. Preclinical mouse MM models of subcutaneous and bone tumors were evaluated using ^{11}C-acetate-PET/CT imaging and tissue biodistribution.

Results—*In vitro*, NMR showed significant uptake of acetate by MMC, and acetate incorporation into intracellular metabolites and membrane lipids. Inhibition of lipid synthesis and acetate transport was toxic to MMC, while sparing resident bone cells or normal B cells. *In vivo*, ^{11}C-acetate uptake by PET imaging was significantly enhanced in subcutaneous and bone MMC tumors compared to unaffected bone or muscle tissue. Likewise, ^{11}C-acetate uptake was significantly reduced in MM tumors after treatment.

Conclusions—Uptake of acetate from the extracellular environment was enhanced in MMC and was critical to cellular viability. ^{11}C-acetate-PET detected the presence of myeloma cells *in vivo*, including uptake in intramedullary bone disease. ^{11}C-acetate-PET also detected response to

Correspondence to: Katherine N. Weilbaecher; Monica Shokeen.

therapy *in vivo*. Our data suggested that acetate metabolism and incorporation into lipids was crucial to MM cell biology and that ^{11}C-acetate-PET is a promising imaging modality for MM.

Introduction

Multiple myeloma (MM) is an age-related malignancy of bone marrow (BM) plasma cells (PC), characterized by the secretion of monoclonal immunoglobulins (Ig) and end-organ damage. MM progression causes profound alterations in bone homeostasis (1), both hyper-activating osteoclast and inhibiting osteoblast activity, and leads to the development of severe multifocal bone disease, associated with high risk of skeletal-related events (SREs) (2–5). Prevention and treatment of complications, effective use of available therapeutics, and the development of new treatments require imaging techniques to efficiently report on tumor localization, extent, and activity of MM lesions after treatment. However, MM bone lesions are not detected by ^{99m}Tc-MDP bone scans due to inhibition of osteoblast activity and apposition of new matrix (5). Skeletal surveys using plain film radiographs of the whole skeleton and CT scans of selected regions and bones are the standard of care. The best currently available positron emission tomography (PET) tracer to image MM tumor metabolic activity and growth is ^{18}F-FDG (fluorodeoxyglucose). In extramedullary lesions ^{18}F-FDG is highly sensitive (96%); however, in intramedullary lesions the sensitivity has been reported to be lower (45.3–76.9, average 61%) (6), possibly because of low glucose uptake in some patients and high uptake by bone resident hematopoietic (7) and osteogenic cells (8).

Preclinical whole body metabolic imaging is a powerful technique to obtain spatiotemporal information on disease evolution, and is a reproducible and translational platform to conduct comparable studies across different models (2, 9). A desirable metabolic tracer for MM should be effective across multiple models, being able to target MM cells (MMC), and differentiate them from the surrounding microenvironment. Bone resident cells mainly rely on glucose as a key metabolic substrate (7, 8). MMC have also been shown to depend on glucose transporters (10); however, we speculated they may also have increased uptake of other substrates to sustain their intense Ig production and replication. In particular, MMC are characterized by a prominent endoplasmic reticulum (ER), the maintenance and replication of which requires the synthesis of significant amounts of membrane lipids, and overexpression of Fatty Acid Synthase (FASN), an ER-resident multi-enzymatic complex that synthesizes long-chain fatty acids from Acetyl-CoA (11, 12). Cells can derive Acetyl-CoA from multiple sources, including the glycolytic end-product pyruvate, and the catabolism of amino-acids and lipids. Some cell types, including astrocytes and hepatocytes (13, 14), can also obtain Acetyl-CoA from the uptake of extracellular monocarboxylic acids such as acetate, a process that cancer cells can exploit to sustain their enhanced metabolic requirements (15). Walters *et. al.* recently showed that MMC collected from patients and established cell lines overexpress monocarboxylate transporters (16), including MCT1, which has been shown to mediate acetate uptake (13, 14).

In this study, we set out to investigate acetate metabolism in MMC, and provide proof-of-principle for its use in metabolic imaging. Our central hypothesis is that MMC would use acetate as a versatile carbon source to sustain their intensive biosynthetic activity,

particularly directing it to *de novo* synthesis of membrane lipids. We, therefore, postulate that acetate uptake would be enhanced in the presence of MMC, and could be exploited to detect and target tumor burden. In the present work, we evaluated acetate uptake *in vitro* in MMC, and *in vivo* in palpable MM cell tumors as well as orthotopic isografts. We tested the sensitivity of ^{11}C-acetate-PET in small animals for detecting engrafted or spontaneous MM, and the efficiency of re-imaging to detect treatment response. We also investigated how myeloma cells utilize acetate uptake to fuel the biosynthesis of cellular components, and can be sensitive to pharmacological manipulation of its metabolism. Taken together, our data show that MMC rely on acetate metabolism, which can be utilized to effectively detect their presence and monitor the response to treatment *in vivo*.

Materials and methods

Cell culture

5TGM1-GFP murine myeloma cell line (5TGM1) was obtained from Dr. G. Mundy (Vanderbilt University, Nashville, TN, USA), and cultured as described previously (17). U266 and OPM2 human myeloma, and ST2 and MC3T mouse stromal cell lines were obtained from ATCC and cultured as recommended by manufacturer.

Animal models

C57Bl/KaLwRij mice (17, 18) were a kind gift from Dr. G Mundy, and bred in-house under specific pathogen-free conditions. NOD.Cg-*Prkdcscid Il2rgtm1Wjl*/SzJ mice (NSG) were purchased from Jackson Laboratories. The Washington University School of Medicine Animal Ethics Committee approved all experiments. For multifocal tumor engraftment, 2–4 month-old male C57Bl/KaLwRij mice were injected with 1×10^6 syngeneic 5TGM1-GFP cells intravenously, which yielded to splenomegaly and significant bone destruction within a month (19). In tumor bearing mice, monoclonal gamma-globulin peak was quantified in the serum protein electrophoresis (SPEP) with a semi-automated analysis software (clinically certified Helena QuickScan 2000 workstation) as previously described (20). Serum from 5TGM1-injected NSG mice (that have no endogenous B-cells) was used as a control for the molecular weight of the band corresponding to the clonal tumor-produced Ig, which will be herein referred to as M-protein. Subcutaneous murine plasma cell tumors (PCT) were established by injecting 1×10^6 5TGM1 in standard matrigel (BD) in the flanks of syngeneic KaLwRij or NSG mice. Xenografts were established by injecting 3.5×10^7 OPM2 or U266 cells in matrigel (BD) supplemented with human IL6 (50 ng/ml, Miltenyi Biotec) in the flank of NSG mice. Bortezomib (1mg/kg) was administered by intravenous injections 5 and 1 days before imaging or biodistribution (d1/d4 protocol, as previously described (21)); melphalan was given weekly at 8mg/kg by intraperitoneal injections.

Optical Imaging

Imaging of GFP-expressing 5TGM1 tumors in mice was performed with the Multispectral FX Pro with planar X-ray (Bruker Biosystems, New Haven, CT). Mice were anesthetized with isoflurane (2% in 100% O_2, v/v) and placed supine on the imaging tray. Brightfield, fluorescence and X-ray images were acquired sequentially without repositioning subjects with 120 mm field of view. GFP fluorescence was detected using 480 nm excitation and 535

nm emission filters with 5 s acquisition time, F-stop 2.4, and 2×2 binning. Fluorescence images were overlaid on brightfield images and ROI analysis performed using NIH ImageJ image processing software.

Small-animal PET imaging

Mice were injected with ^{11}C-acetate (~11 MBq) by tail vein prior to performing 0–60 min dynamic PET scans. Small animal PET images were acquired with microPET Focus 220 scanner (Concorde Microsystems Inc., Knoxville, TN), or with Inveon microPET/CT scanner (Siemens Medical Solutions, Washington D.C.), while the CT images were acquired with the Inveon. Both scanners are cross-calibrated per established standard operating procedure. Inveon Research Workstation (IRW) software (Siemens) was used for image analysis. Regions of interest (ROI) were selected from maximum intensity projection (MIP) PET images using CT anatomical guidelines and the activity associated with ROIs were derived from the IRW. For comparative ^{11}C-acetate/^{18}F-FDG PET studies, mice were anesthetized under 1% isoflurane and placed prone on the imaging platform of the Focus 220 or Inveon. ^{11}C-acetate was administered as a bolus dose of ~11 MBq/mouse *via* a tail vein catheter and dynamic whole body images were captured over 30 minutes post injection of the contrast. ^{18}F-FDG imaging was performed ~4 h after ^{11}C-acetate imaging. Mice were anesthetized again under isoflurane and placed prone in the Inveon microPET/CT. ^{18}F-FDG was administered as a bolus dose of 9 MBq/mouse by tail vein catheter and dynamic PET/CT whole body images were collected over 60 minutes. Maximum standard uptake values (SUVs) were calculated using the equation: SUV=([nCi/mL]x[animal weight (g)]/[injected dose (nCi)]). Corresponding time activity curves (TACs) were plotted and analyzed with IRW.

Animal bio-distribution

For bio-distribution studies, animals were sacrificed 1 h after ^{11}C-acetate (~11 MBq) injection. Organs of interest were harvested, weighted and counted in the gamma counter. The percentage injected dose per gram of tissue (%ID/g) was determined by decay correction of the radiopharmaceutical for each sample normalized to a standard of known weight, which was representative of the injected dose. In order to compare different experiments, each sample's %ID/g was divided by the %ID/g of blood from the same animal.

Flow Cytometry

Viable cells were obtained from mechanically dissociated spleens, collagenase-digested tumors or bone marrow flush, washed in FACS buffer, stained, and immediately analyzed with FACS Calibur (BD) or Canto (BD). Flow cytometry data were analyzed with FlowJo. For GFP+ tumor graft viability, 7-aminoactinomycin D (7AAD) or Propidium Iodide (PI) negative/GFP-positive population was considered as viable tumor cells and used for statistical analysis. In order to characterize the development of spontaneous MM, spleens and BM were stained with anti-CD138-APC antibodies (BD).

Sample Preparation for NMR Measurement

For studies on extracellular media, 5TGM1, OPM2 and U266 cells were incubated in the presence of 0.005–0.01 M ^{13}C-acetate in standard growth media at a concentration of 10^6 cells/mL (−/+0.35). At the indicated time-points supernatants and cell pellets were snap-frozen, and analyzed by NMR as described in supplementary methods. Briefly, cell growth media was lyophilized, re-suspended into D_2O with 1 mM t-butanol as an internal standard, adjusted to a pH of 7.0 and then loaded into 5 mm tubes for NMR analysis. Intracellular metabolites were obtained with organic solvent extraction (methanol/water and chloroform) as previously described (22, 23). Metabolites from the aqueous layer were re-suspended into D_2O with 1 mM t-butanol and charged into a susceptibility-matched Shigemi tube. Metabolites from the chloroform fraction (membrane extraction) were re-suspended in 0.6 mL deuterated chloroform. NMR measurements with Car-Purcell-Meiboom-Gill (CPMG) and gradient Heteronuclear Single Quantum Coherence (gHSQC) methods were carried out at RT using a DD-II 11.75 tesla spectrometer (Agilent/Varian). Free Induction Decay (FID) values were multiplied by a gaussian adapodization function with a 0.1 s time constant. For the ^{1}H-^{13}C gHSQC 2D experiment measurement on lipid layer from cell extractions, spectral width was 8012 Hz for ^{1}H and 31250 Hz for ^{13}C, and the FID was manipulated *via* an apodization function consisting of a negative exponential and 0.05 Hz Gaussian function. Spectra were processed with VnmrJ 4.2A software with Agilent CRAFT (Complete Reduction to Amplitude-Frequency Table) to calculate the relative amplitude of substrates or metabolites (see supplementary methods).

In vitro assays

For *in vitro* cytotoxicity assays, orlistat (Cayman) and α-cyano-4-hydroxycinnamic acid (CHC, Sigma) or vehicles (ethanol and dimethyl sulfoxide, DMSO, respectively) were added to cell cultures, and cell death was measured by flow cytometry after PI staining, or with AnnexinV-PE and 7-AAD apoptosis detection kit (BD). Spleen cells were obtained from mechanical dissociation of adult C57BL/6 mice spleens, cultured in RPMI1640 10% FBS, β-mercaptoethanol 50 mM, sodium pyruvate (1mM), glutamine (2mM) (Sigma), in the presence or absence of CHC (1–5mM) and/or Orlistat (50–200μM). CD45 positive selection was performed with magnetic beads (Milteni). Cell viability was analyzed by trypan blue, B cell viability was assessed by FACS upon staining with 7AAD, CD19-PE (BD) and CD45-APC (BD). Bone marrow monocytes (BMM) and stromal cells (BMSC) were obtained by flushing long bones of adult C57BL/6 mice, and cultured as previously described (24, 25). To generate osteoclasts, BMM cultures were stimulated with 50 ng/mL M-CSF, and 30 ng/mL RANKL for 6 days, then stained for TRAP using the leukocyte acid phosphatase kit (Sigma) (24, 25). BMSC or the BMSC cell line ST2 were induced to differentiate into adipocytes and stained with Oil-Red-O as previously described (25). Formation of mineralized matrix upon osteogenic differentiation was assessed by Alizarin Red staining (25). In all differentiation assays, orlistat at the indicated concentrations was administered starting on the first day of differentiation and re-supplemented with every media change (every 2–3 days for 2–3 weeks).

Statistical Analysis

Statistical analyses were performed using Prism5 (GraphPad). Group comparison experiments were analyzed using student t test or analysis of variance (ANOVA). Bar graphs represent means and errors bars represent standard deviations (SD). Correlation analyses were performed using Pearson's correlation (r) for normally distributed datasets, and Spearman's rank correlation (rs) when a Gaussian approximation of the distribution could not be expected (biodistribution or treatment experiments). Results were considered to reach significance at $p \leq 0.05$.

Results

Metabolite fate tracking by NMR shows metabolism of extracellular acetate by myeloma cells

In order to evaluate uptake of acetate and its metabolism by MMC we performed ^{1}H-NMR and ^{13}C-edited ^{1}H NMR experiments. Three MM cell lines (5TGM1, OPM2 and U266) were incubated with ^{13}C-labeled acetate, and ^{1}H-NMR CPMG experiments were performed on the spent media and cellular extracts. ^{1}H-NMR analysis at different time-points (Fig. 1A–C) showed a time-dependent decrease of acetate in the extracellular media, evident after a few hours of incubation (Fig. 1A). As expected, glucose was decreased as well (Fig. 1B), while extracellular lactate increased over time, consistently with active production by MMC (Fig. 1C). Analysis of spent media by ^{1}H-NMR after incubation with acetate of different concentrations of cells for 5h also showed that extracellular acetate and glucose decreased with increasing cell concentration, while extracellular lactate increased (Supplementary Fig. 1 A–C). These experiments demonstrated direct uptake of extracellular acetate by MM cells.

In order to analyze the cellular metabolism by MMC and the fate of extracellular acetate, we incubated over time 5TGM1, OPM2 and U266 cells with ^{13}C-acetate, obtained aqueous extracts from lyophilized cell pellets, and analyzed by HSQC NMR using t-butanol as an internal standard (peak #1 in Fig. 1D). ^{13}C-labeled acetate peaks were identified by both CPMG and HSQC at 1.91 ppm (peak #2 Fig. 1D) in MMC extracts consistent with cellular acetate uptake (26). Importantly, we found evidence of intracellular acetate metabolism through ^{13}C-labeling of a number of other compounds, mostly in peaks consistent with -CH_2- in groups at chemical shifts of 2.07 ppm (peak #3, 3-glutamate) (26), 2.35–2.37 ppm (peak #4, 4-glutamate)(26), and 2.53 ppm (glutathione, GSH) (27) (assignments listed in Fig. 1D). A peak at 3.21–3.23 ppm, suggestive of a trimethyl group, was identified as phosphocholine by spiking authentic standard into cell extracts and performing 2D-NMR (not shown). This peak was evident in all MM cellular extracts in ^{13}C-gHSQC spectra (peak #7 Fig. 1D), though it might be due to the high abundance of phosphocholine, as reflected in its high representation from ^{1}H-CPMG measurements (see Fig. 1D). Specific enrichment for labeled ^{13}C from acetate was directly demonstrable by comparing calibrated glutamate integrals in gHSQC and CPMG, and verifying a significant increase over time in U266 and OPM2 cells ($p<0.01$, Supplementary Fig. 1E). Together these data demonstrated that MMC readily uptake and metabolize extracellular acetate.

In order to assess the contribution of acetate toward the biosynthesis of lipid rich cellular membranes, MM cell lines were incubated with ^{13}C-acetate for 70h, allowing for long-term anabolic processes to occur. 2D NMR analysis of water-insoluble intracellular membrane extracts showed that all cell lines had substantial incorporation of ^{13}C-labeled carbons. Consistent with what we observed in the water-soluble cytosolic extracts, OPM2 and U266 had high levels of labeled ^{13}C in the water insoluble fraction of intracellular metabolites at frequencies corresponding to hydoxybutyrate (Peak #3, Fig. 1E), to a trymethylaminic group compatible with phosphocholine (Peak #4 at 3.21ppm, ^{1}H Fig. 1E), and -CH- groups compatible with the C in position 2 of the glycerol backbone of phospholipids. Notably, all three MMC lines showed a robust signal for ^{13}C incorporation into -CH_2- groups and -CH_3 (25–40 ppm ^{13}C, 1.32–1.35 ppm ^{1}H), suggesting that a relevant fraction of internalized acetate contributed to the synthesis of fatty acid chains (-C-$(CH_2)_n$-CH_3) (Fig. 1E and Supplementary Fig. 1F)(28). These data show that myeloma cell lines utilize extracellular acetate in the synthesis of fatty acid chains and phospholipids, which are key steps in *de novo* biosynthesis of membrane lipids (see working model Fig. 2A).

Pharmacological inhibition of acetate metabolism decreases viability of MM cells

We found that MMC take up acetate from extracellular environment and utilize acetate in anabolic pathways including the synthesis of membrane lipids. We next evaluated whether inhibition of acetate transport and metabolism impacted MMC viability (Fig. 2A). It has been demonstrated that MMC express the monocarboxylate transporter MCT1 (16) (Fig. 2A). To inhibit extracellular import of acetate, we used the MCT1 inhibitor α-cyano-4-hydroxycinnamic acid (CHC), at doses (0.5–5mM) that have been reported to inhibit MCT1 transport activity *in vitro* (14). By vital staining, we found that CHC induced dose-dependent cell death in MMC (Fig. 2B). We also found that the same low-millimolar dosage blunted ^{13}C-acetate uptake from the extracellular media as well as its incorporation in intracellular metabolites using ^{13}C-edited ^{1}H-NMR (8h, 2.5 mM) (Supplementary Fig. 2A).

Having found that MMC were sensitive to inhibition of acetate transport using a MCT1 inhibitor (CHC), we next evaluated effects of blocking acetate incorporation into membrane long-chain fatty acids (-$^{13}CH_2$- and $^{13}CH_3$) (precursors to membrane biogenesis (11, 27)), by using the FASN inhibitor orlistat (Fig. 2A and 2C). MMC underwent dose- (Fig. 2C, Supplementary Fig. 2B) and time-dependent cell death (Supplementary Fig. 2C) after orlistat administration. However, orlistat had little effect on viability of non-malignant splenocytes (Fig. 2D). To further assess specificity for MMC, we isolated primary bone marrow cells and performed osteoblast, osteoclast and adipocyte differentiation assays. As expected, orlistat (20–100 μM) prevented adipogenic differentiation of primary murine bone marrow stromal cells (BMSC) (Supplementary Fig. 2D) and adipogenenic differentiation of bone marrow stromal cell line ST2 (Fig. 2E). However, Oil-Red-O negative-viable cells were still present after long-term treatment (Fig. 2E), suggesting that loss of *in vitro* adipogenesis was due to a block of differentiation rather than death of precursors. Orlistat failed to induce apoptosis in bone marrow stromal cell lines (ST2 and MCT3) or in primary murine BMSC (Supplementary Fig. 2E). Likewise, orlistat had little effect on osteoclast differentiation of bone marrow monocytes, stimulated with M-CSF and RANKL (Fig. 2F). Finally, orlistat did not inhibit osteoblast differentiation even after long-term exposure (20

days, 20–50 μM orlistat) (Fig 2G). Thus, blockade of FASN with orlistat significantly decreased MM cell viability and inhibited adipogenesis, but had little effect on the viability and differentiation of BMSC, osteoblasts, and osteoclasts.

We next tested whether combined inhibition of acetate uptake (CHC) and acetate metabolism (orlistat) would enhance anti-MM activity. We treated 5TGM1 or non-tumor CD45+ splenocytes with orlistat, alone or in combination with CHC (2mM), and assessed viability (Fig. 2D). In 5TGM1 MMC there was a significant decrease in viability upon treatment with orlistat ($p<0.01$) that was enhanced by CHC (interaction $p<0.05$ by two-way ANOVA). Non-tumor splenocytes, by contrast, showed no significant decrease of viability with any of the treatments (Fig. 2D). Specific effects on normal B cells were further tested by treating splenocyte cultures for 48h, then staining for B cell markers. Flow cytometry showed no significant difference in the percentage of CD45+/CD19+/7AAD− cells in cultures treated with CHC and/or orlistat relative to vehicle (Fig. 2H). Human MMC lines U266 and OPM2, as well as murine 5TGM1 cells, underwent increased cell death upon combined treatment with orlistat (24–48h 20 or 50 μM) and CHC (500 μM to 5 mM) (Fig. 2I and Supplementary Fig. 2F–H). Importantly, the same doses of CHC and orlistat failed to induce relevant cell death in mouse primary BMSC (Fig. 2I). Together, these data suggest that anabolic metabolism of acetate plays a significant role in MMC biology, and support the hypothesis that acetate uptake may be robustly enhanced in the presence of MMC.

MM plasma cell tumors (PCT) have avidity for ^{11}C-acetate *in vivo*

In order to assess acetate uptake *in vivo*, we established 5TGM1 subcutaneous plasma cell tumors (PCT) in syngeneic immunocompetent KaLwRij mice, injected ^{11}C-acetate intravenously (i.v.) in tumor-bearing or control mice, and performed a tissue bio-distribution assay one hour after injection. Briefly, we used %ID (injected dose)/g from un-metabolized radiolabeled acetate, as well as byproducts such as CO_2, in the circulating blood as normalization factor, and compared tumor uptake to muscle (a skeletal tissue non affected by tumor infiltration), in tumor-bearing as well as control mice. We found that muscle samples had equal acetate uptake in tumor- and non-tumor bearing mice (average fold increase relative to circulating blood of 1.8 vs. 1.6, SD 0.5 vs. 0.3), while 5TGM1 PCT had enhanced ^{11}C-acetate uptake (3.3, SD 0.5, $p<0.01$) (Fig. 3A). As expected, normalized total tissue uptake correlated with tumor weight ($p<0.01$, $r=0.84$). As tumors consist of mixed cell populations and can have large necrotic and/or hemorrhagic areas, we measured the percentage of viable MMC in each tumor and compared them with the radiotracer uptake. Post biodistribution, tumors were collagenase-digested, stained for dead cells with 7AAD, and analyzed by flow cytometry. Importantly, we found that the percentage of GFP+ 7AAD − viable tumor cells directly correlated with weight-normalized ^{11}C-acetate uptake in the tumor tissue ($p<0.01$, $r=0.8$, Fig. 3B). This suggested that enhanced uptake was directly related to the presence of viable tumor cells in the tissue.

We then imaged 5TGM1 tumors using GFP imaging and ^{11}C-acetate-PET imaging. We found that MM tumors were readily detected by both GFP and ^{11}C-acetate-PET imaging (Fig. 3C, Supplementary Fig. 3A). As expected, there was uptake of ^{11}C-acetate in non-tumor abdominal organs, consistent with the role of acetate metabolism in the liver (29), the

gut microbiota (30), and spleen (29). However, time-activity curves showed avid uptake of ^{11}C-acetate in the PCT, which was significantly higher compared to the surrounding uninvolved muscle tissue (Fig. 3C–D). 5TGM1 MMC have been reported to have high ^{18}F-FDG-PET uptake *in vivo* (31). Accordingly, our *in vitro* metabolite fate tracking demonstrated that 5TGM1 cells take up both glucose and acetate (Fig. 1 and Supplementary Fig. 1). We therefore evaluated ^{11}C-acetate-PET and ^{18}F-FDG-PET imaging in the same tumor bearing mice. We performed ^{18}F-FDG-PET imaging three hours after imaging with ^{11}C-acetate-PET of 5TGM1 bearing mice (Fig. 3E=, supplementary Fig. 3B). We then measured the areas of increased uptake with each modality, and found a very strong correlation in the tumor areas measured with ^{11}C-acetate and ^{18}F-FDG ($r=0.98$ $p<0.01$) (Fig. 3F), suggesting that both modalities imaged MMC *in vivo*.

We next evaluated *in vivo* ^{11}C-acetate uptake by a second MMC line, human U266, using PET-CT and tissue biodistribution. ^{11}C-acetate small animal PET-CT (Fig. 3G) and ^{11}C-acetate biodistribution (Fig. 3H) showed enhanced ^{11}C-acetate uptake in human myeloma U266 tumors relative to the surrounding tissues. Inoculation of another human myeloma cell line, OPM2, also showed higher ^{11}C-acetate uptake compared to muscle by bio-distribution assay (Supplementary Fig. 3C). Thus, human and mouse MMC exhibit enhanced ^{11}C-acetate uptake relative to surrounding tissues.

^{11}C-acetate uptake *in vivo* is increased in tumor bearing bones

5TGM1 cells induce anemia, detectable serum IgG2bk M-protein (measured by ELISA (19, 21, 32) or SPEP(32–34)), renal failure (as seen in human MM), and bone lesions, when inoculated i.v. in KaLwRij mice (9, 18, 19, 24, 35). After injecting 5TGM1 i.v., GFP+ cells were found to localize to the bones by *ex-vivo* optical imaging (Supplementary Fig. 3D), and tumor burden was quantified by *ex vivo* bone marrow flow cytometry. While very few GFP positive cells were found in the bone marrow of subcutaneously inoculated mice, high numbers were detectable in i.v. injected KaLwRij ($p<0.01$) (Supplementary Fig. 3E–F). ^{11}C-acetate-PET showed enhanced uptake in the tumor bearing bones of 5TGM1 mice. Semi-quantitative standard uptake values (SUV) and time-activity curves revealed rapid and significantly increased uptake in 5TGM1 tumor-bearing bones compared to non-tumor bearing KaLwRij mice ($p=0.05$, Fig. 4 A–B). Tissue biodistribution demonstrated significantly higher ^{11}C-acetate uptake in tumor bearing bones, as compared to muscle, or to the bones of mice bearing extra-skeletal 5TGM1 tumors ($p<0.01$, Supplementary Fig. 3F).

KaLwRij mice upon aging can develop MGUS (monoclonal gammopathy of undetermined significance), with a time-dependent risk of progression that strongly resembles human myeloma (1% per year). ^{11}C-acetate-PET imaging was performed on an aged KaLwRij mouse (1 year old) that had developed detectable monoclonal component by SPEP, and on an age-matched KaLwRij mouse that had no detectable monoclonal gammopathy. PET images showed areas of increased ^{11}C-acetate uptake throughout the skeleton of the M-protein positive mouse (Fig. 4 C–D). Importantly, staining for plasma cell marker CD138 and flow cytometric analysis of bone marrow revealed 20% of CD138^{pos} plasma cells (vs. 2% and 3% respectively in an age-matched KaLwRij and C57Bl/6 – black 6) consistent with the pathological criteria for MM diagnosis in humans. Staining of spleen cells also showed

68% CD138^{pos} cells (vs. 4% and 15% of controls), further suggesting active plasma cell dyscrasia (Fig. 4E). These data show that ^{11}C-acetate-PET imaging can detect skeletal tumor burden in a mouse with spontaneous MM.

^{11}C-acetate uptake decreases consistently with MM cell death shortly after treatment

A significant therapeutic goal for metabolic imaging in cancer is to rapidly detect response to treatment. We therefore treated 5TGM1-inoculated KaLwRij mice with clinically available anti-myeloma agents, and evaluated acetate uptake *in vivo* before we would expect changes with standard assessments of tumor burden. We established subcutaneous 5TGM1 tumors and treated mice with the proteasome inhibitor bortezomib (i.v. on day 1 and 4), and, after only 5 days of therapy, evaluated the response to treatment by ^{11}C-acetate uptake. Tissue biodistribution post ^{11}C-acetate injection was performed one day after the second injection of bortezomib (day 5), followed by analysis of tumor weight and MM cell viability from excised tumors by flow cytometry. As expected, after only 5 days of therapy, there was no change in the size of tumors as quantitated by bi-directional caliper measurements and tumor weights between vehicle and bortezomib treated mice (data not shown). However, we did detect decreases in ^{11}C-acetate uptake from the bortezomib-treated tumors compared to the vehicle-treated tumors ($p<0.05$, Fig. 5A). *Ex vivo*, flow cytometry of the tumor tissue showed a higher percentage of dead cells (Supplementary Fig. 4A), and a lower percentage of viable GFP+ tumor cells (Fig. 5B $p<0.01$) in the bortezomib treated animals, consistent with a response to treatment. We found a direct correlation between ^{11}C-acetate uptake and the percentage of viable cancer cells in the subcutaneous PCT ($rs=0.7$, $p=0.02$, Supplementary Fig. 4B).

We next evaluated if ^{11}C-acetate-PET would show differences in tumor uptake in mice treated with a different class of anti-myeloma therapy and at later time points. We imaged mice with 5TGM1 subcutaneous PCT after treatment with an alkylating agent, melphalan. After 2 weeks of melphalan therapy, ^{11}C-acetate-PET showed significantly decreased SUV_{max} ($p<0.05$) and tumor ROI area ($p<0.01$) in melphalan versus vehicle-treated controls (Fig. 5C). Accordingly, tumor weight was lower in melphalan- relative to vehicle-treated mice (average 0.5 vs. 1.2g, $p<0.01$), and flow cytometry of mechanically and enzymatically dissociated tumors showed higher cell death and lower tumor cell viability ($p<0.05$ Fig. 5D).

Finally, we evaluated serial ^{11}C-acetate-PET to detect early treatment response to 5 days of bortezomib in bone-residing MM tumors. At three weeks, a clear monoclonal component was evident as a distinct band in the γ-globulin region by SPEP; baseline ^{11}C-acetate-PET was performed, and demonstrated high uptake in the tibiae (Fig. 5 E–F). Mice where then dosed with bortezomib i.v. on day 1/day 4, and re-imaged with ^{11}C-acetate-PET 1 day after the second dose (day 5, Fig. 5 E–F). ^{11}C-acetate-PET showed a significant reduction in the tibia SUV relative to baseline scans ($p<0.01$, Fig. 5F). Quantitation of SPEP measurements showed significantly lower Ig than in vehicle-treated controls (supplementary Fig. 4F $p=0.03$). The circulating IgG2b half-life in a mouse is 4–6 days(36); accordingly, after only 5 days of therapy, the M-protein band was still detectable on the SPEP blot in treated animals (Fig. 5G). However, bortezomib vs. vehicle-treated animals had fewer viable GFP+ tumor cells in the bone marrow (98% reduction, Supplementary Fig. 4E $p<0.01$). Together,

these data showed that a decrease in ^{11}C-acetate uptake by PET correlated with decreased tumor cell viability, suggesting that ^{11}C-acetate PET can detect treatment responses in models of soft tissue and bone MM.

Discussion

MM is a plasma cell malignancy associated with anemia, renal failure, and extensive bone destruction. Diagnosis and evaluation of treatment response in MM rely on a number of specific and reliable serum biomarkers, including M-component by serum or urine electrophoresis (SPEP or UPEP), free light chain (sFLC), β2-microglobulin (3), and more novel analytes, such as serum B-cell maturation antigen (37). As 70–90% of MM patients develop osteolytic lesions (38) and are at high risk of SREs (4, 5), imaging techniques are also required to provide spatial information on bone disease, which complement systemic biomarkers in diagnostics and aid in the management of SREs. In particular, metabolic imaging facilitates the identification and monitoring of skeletal sites of tumor activity. Metabolic imaging can differentiate metabolically active tumor lesions from large osteolytic areas where tumor cells may have been cleared by therapy but bone regeneration has not yet occurred as seen by standard radiographic imaging. Functional PET imaging of MM tumor-metabolism using ^{18}F-FDG has been widely used in the clinic for staging, treatment planning, and monitoring of response (39, 40). Despite the impressive results of ^{18}F-FDG on prognosis and treatment response, studies have suggested that other metabolic tracers are needed to complement ^{18}F-FDG (38). While MMC show a variable degree of GLUT-1 expression (10), the dependence on glucose metabolism by other cell types in the bone microenvironment (7, 8) may confound imaging by ^{18}FDG-PET (6, 41).

^{11}C-acetate PET was recently shown to have a high sensitivity of detection of bone lesions in patients with MM and prostate cancer (42–44). As metabolic imaging relies on characteristic features in the metabolism of cancer cells relative to the surrounding non-tumor tissues(45), in the present study we investigated the role of acetate metabolism in MM. Using metabolite fate tracking with ^{13}C-edited ^{1}H-NMR, we found in 3 different MMC lines that acetate in the extracellular media decreases proportionally to the increase in cell concentration and time of incubation, suggesting active uptake by MMC. In line with findings from studies on the NS0 cell line (46), we also found evidence of rapid incorporation of ^{13}C-acetate into glutamate, which could derive from the TCA-intermediate α-ketoglutarate. Allowing more time for anabolic processes to occur, we noticed ^{13}C incorporation from extracellular acetate into membrane lipids, a process consistent with FASN activity (11, 42).

In MMC, as in normal PC, an ample part of the cytoplasm is occupied by a prominent, lipid-rich, endoplasmic reticulum (ER), the double-membrane organelle responsible for the synthesis of membranes and secretory proteins (such as Ig). Within 48h of activation, a B cell differentiating into plasma cell increase the synthesis of phosphocholine alone by 500–700% (47, 48). The transcription factor XBP-1, a master regulator of both PC differentiation and MMC survival, mediates this process (48) by upregulating a number of enzymes involved in lipid metabolism, such as FASN, which is also overexpressed by MMC (49). Recent studies in prostate cancer have shown that FASN activity could drive the uptake of

acetate from the extracellular environment, which resulted in tumor uptake that was imaged by PET (50). We found that extracellular acetate was readily incorporated into membrane lipids in MM cells and that blockade of FASN with orlistat decreased MMC viability. A recent study on patient MMC and cell lines demonstrated upregulation of MCT1, a primary acetate transporter (13, 46). Accordingly, we found that MMC were sensitive to inhibitors of extracellular acetate transporters (CHC) or of FASN (orlistat), alone or in combination, at doses that did not affect viability of normal B cells or of normal bone cells (BMSC, osteoblasts, osteoclasts). Taken together, our observations suggest that acetate is involved in key metabolic functions in MMC, and could represent a candidate for new therapies, and a robust target for imaging.

Molecular imaging can be used to complement morphological imaging by informing on viability or activity of tumor cells, ideally differentiating lesions with actively proliferating tumor cells, which would be more likely to require additional treatment over the short term, from sites with necrotic tumor cells or unhealed large bone defects. In this study, we addressed ^{11}C-acetate as a potential PET imaging radiotracer in MM, and found ^{11}C-acetate uptake *ex-vivo* (biodistribution) and *in vivo* in a number of myeloma mouse models. Our results show a consistent increase in the uptake of radiolabeled ^{11}C-acetate in the presence of MMC *in vivo*, with a clear increase relative to surrounding tissues, and a quantifiable difference between tumor bearing and control mice. In the genetically-labeled (GFP+), glucose-avid model of subcutaneous 5TGM1 tumors (31), ^{11}C-acetate- PET imaging identified the same tumor area as the bench-mark imaging techniques for this model: ^{18}F-FDG-PET and optical (GFP) imaging. Importantly, enhanced ^{11}C-acetate uptake was also demonstrated in MM tumors from non-fluorescently-labeled human cell lines (U266 and OPM2), and in bone-localizing MM, both in the orthotopic multifocal 5TGM1 model (i.v. in KaLwRij) and in a spontaneous MM evolved from MGUS. Despite the challenges of imaging small animals, where bone lesions have diameters of few millimeters or smaller, ^{11}C-acetate-PET was able to show increased uptake in tumor bearing mice, and a decrease in uptake following treatment that was proportional to MM cell death. Unlike human disease, where MM localizes primary to bones, the KaLwRij model also presents prominent tumor engraftment to the spleen: in small animal imaging we found that high splanchnic uptake interfered with detection of tumor burden in this extra-skeletal site. In clinical settings, however, imaging studies with ^{11}C-acetate-PET have shown the capability of this method to detect prostate cancer metastases to abdominal lymph nodes (51), as well as lumbar vertebrae (44), suggesting that the splanchnic background may be less relevant in humans. Specifically in MM, a first set of studies (42, 43) have shown good sensitivity and specificity of ^{11}C-acetate-PET in patients, without major interference of abdominal uptake. (42).

In all, our data show proof-of-concept evidence that directly links a survival mechanism of MMC to their consistent uptake of acetate *in vitro* and *in vivo*, which allows assessment of tumor burden by ^{11}C-acetate-PET imaging. Although further studies will be needed to demonstrate whether ^{11}C-acetate-PET is superior or complementary to other molecular imaging methods, our study provides mechanistic and preclinical evidence in support of future studies to explore the role of acetate metabolism as potential therapeutic target in MM, and proof-of-concept evidence for the development of this imaging technique in MM.

Supplementary Material

Refer to Web version on PubMed Central for supplementary material.

Acknowledgments

The authors wish to thank Drs. Michael Tomasson, Samuel Achilefu, Michelle Hurchla and Marcus Watkins for their suggestions and valuable criticisms. We thank the Teitelbaum Lab members, Gail Sudlow, Yalin Xu, Lan Lu for their expert technical assistance. We are deeply grateful to Drs. Nicola Napoli, Silvia Mari and Jose Garcia Manteiga for their wonderful training and expert suggestions regarding metabolomics. This research was primarily funded by the NIH CTSA Grant # UL1 TR000448 and R01-CA176221. We thank the Center for Multiple Myeloma Nanotherapy (CMMN) U54CA199092, Musculoskeletal Research Center for histology (NIH P30 AR057235), the MIR pre-clinical PET/CT and the cyclotron facility, the P50 small animal imaging core for optical imaging (CA94056) and Washington University high Resolution NMR Facility (the HIH Shared Instrument Grant S10 RR027184). We thank the support provided by the Men's Group Against Cancer, NIH CA097250, R01-DK085298, R01-CA176221, NIH CA097250, PPG CA100730, CA154737-01. F.F. was supported by the Young Investigator Programme 2013 Fondazione Umberto Veronesi.

References

1. Kawano Y, Moschetta M, Manier S, Glavey S, Gorgun GT, Roccaro AM, et al. Targeting the bone marrow microenvironment in multiple myeloma. Immunological reviews. 2015; 263:160–72. [PubMed: 25510276]
2. Terpos E, Berenson J, Raje N, Roodman GD. Management of bone disease in multiple myeloma. Expert review of hematology. 2014; 7:113–25. [PubMed: 24433088]
3. Bianchi G, Anderson KC. Understanding biology to tackle the disease: Multiple myeloma from bench to bedside, and back. CA: a cancer journal for clinicians. 2014; 64:422–44. [PubMed: 25266555]
4. Saad F, Lipton A, Cook R, Chen YM, Smith M, Coleman R. Pathologic fractures correlate with reduced survival in patients with malignant bone disease. Cancer. 2007; 110:1860–7. [PubMed: 17763372]
5. Roodman GD. Pathogenesis of myeloma bone disease. Leukemia. 2009; 23:435–41. [PubMed: 19039321]
6. Lu YY, Chen JH, Lin WY, Liang JA, Wang HY, Tsai SC, et al. FDG PET or PET/CT for detecting intramedullary and extramedullary lesions in multiple Myeloma: a systematic review and meta-analysis. Clinical nuclear medicine. 2012; 37:833–7. [PubMed: 22889770]
7. Baumann K. Stem cells: A metabolic switch. Nature reviews Molecular cell biology. 2013; 14:64–5.
8. Esen E, Chen J, Karner CM, Okunade AL, Patterson BW, Long F. WNT-LRP5 signaling induces Warburg effect through mTORC2 activation during osteoblast differentiation. Cell metabolism. 2013; 17:745–55. [PubMed: 23623748]
9. Paton-Hough J, Chantry AD, Lawson MA. A review of current murine models of multiple myeloma used to assess the efficacy of therapeutic agents on tumour growth and bone disease. Bone. 2015; 77:57–68. [PubMed: 25868800]
10. McBrayer SK, Cheng JC, Singhal S, Krett NL, Rosen ST, Shanmugam M. Multiple myeloma exhibits novel dependence on GLUT4, GLUT8, and GLUT11: implications for glucose transporter-directed therapy. Blood. 2012; 119:4686–97. [PubMed: 22452979]
11. Wakil SJ. Fatty acid synthase, a proficient multifunctional enzyme. Biochemistry. 1989; 28:4523–30. [PubMed: 2669958]
12. Wang WQ, Zhao XY, Wang HY, Liang Y. Increased fatty acid synthase as a potential therapeutic target in multiple myeloma. Journal of Zhejiang University Science B. 2008; 9:441–7. [PubMed: 18543396]
13. Rae C, Fekete AD, Kashem MA, Nasrallah FA, Broer S. Metabolism, compartmentation, transport and production of acetate in the cortical brain tissue slice. Neurochemical research. 2012; 37:2541–53. [PubMed: 22851350]

14. Waniewski RA, Martin DL. Preferential utilization of acetate by astrocytes is attributable to transport. The Journal of neuroscience: the official journal of the Society for Neuroscience. 1998; 18:5225–33. [PubMed: 9651205]
15. Kamphorst JJ, Chung MK, Fan J, Rabinowitz JD. Quantitative analysis of acetyl-CoA production in hypoxic cancer cells reveals substantial contribution from acetate. Cancer & metabolism. 2014; 2:23. [PubMed: 25671109]
16. Walters DK, Arendt BK, Jelinek DF. CD147 regulates the expression of MCT1 and lactate export in multiple myeloma cells. Cell Cycle. 2013; 12:3175–83. [PubMed: 24013424]
17. Dallas SL, Garrett IR, Oyajobi BO, Dallas MR, Boyce BF, Bauss F, et al. Ibandronate reduces osteolytic lesions but not tumor burden in a murine model of myeloma bone disease. Blood. 1999; 93:1697–706. [PubMed: 10029599]
18. Radl J, Hollander CF, van den Berg P, de Glopper E. Idiopathic paraproteinaemia. I. Studies in an animal model--the ageing C57BL/KaLwRij mouse. Clinical and experimental immunology. 1978; 33:395–402. [PubMed: 367647]
19. Oyajobi BO, Franchin G, Williams PJ, Pulkrabek D, Gupta A, Munoz S, et al. Dual effects of macrophage inflammatory protein-1alpha on osteolysis and tumor burden in the murine 5TGM1 model of myeloma bone disease. Blood. 2003; 102:311–9. [PubMed: 12649140]
20. Soodgupta D, Zhou H, Beaino W, Lu L, Rettig M, Snee M, et al. Ex Vivo and In Vivo Evaluation of Overexpressed VLA-4 in Multiple Myeloma Using LLP2A Imaging Agents. Journal of nuclear medicine: official publication, Society of Nuclear Medicine. 2016; 57:640–5.
21. Hurchla MA, Garcia-Gomez A, Hornick MC, Ocio EM, Li A, Blanco JF, et al. The epoxyketone-based proteasome inhibitors carfilzomib and orally bioavailable oprozomib have anti-resorptive and bone-anabolic activity in addition to anti-myeloma effects. Leukemia. 2013; 27:430–40. [PubMed: 22763387]
22. Beckonert O, Keun HC, Ebbels TM, Bundy J, Holmes E, Lindon JC, et al. Metabolic profiling, metabolomic and metabonomic procedures for NMR spectroscopy of urine, plasma, serum and tissue extracts. Nature protocols. 2007; 2:2692–703. [PubMed: 18007604]
23. Matheus N, Hansen S, Rozet E, Peixoto P, Maquoi E, Lambert V, et al. An easy, convenient cell and tissue extraction protocol for nuclear magnetic resonance metabolomics. Phytochemical analysis: PCA. 2014; 25:342–9. [PubMed: 24453161]
24. Heller E, Hurchla MA, Xiang J, Su X, Chen S, Schneider J, et al. Hedgehog signaling inhibition blocks growth of resistant tumors through effects on tumor microenvironment. Cancer research. 2012; 72:897–907. [PubMed: 22186138]
25. Watkins M, Grimston SK, Norris JY, Guillotin B, Shaw A, Beniash E, et al. Osteoblast connexin43 modulates skeletal architecture by regulating both arms of bone remodeling. Molecular biology of the cell. 2011; 22:1240–51. [PubMed: 21346198]
26. Gribbestad IS, Petersen SB, Fjosne HE, Kvinnsland S, Krane J. 1H NMR spectroscopic characterization of perchloric acid extracts from breast carcinomas and non-involved breast tissue. NMR in biomedicine. 1994; 7:181–94. [PubMed: 7946996]
27. Guidoni L, Ricci-Vitiani L, Rosi A, Palma A, Grande S, Luciani AM, et al. 1H NMR detects different metabolic profiles in glioblastoma stem-like cells. NMR in biomedicine. 2014; 27:129–45. [PubMed: 24142746]
28. Lee CW, Griffin RG. Two-dimensional 1H/13C heteronuclear chemical shift correlation spectroscopy of lipid bilayers. Biophysical journal. 1989; 55:355–8. [PubMed: 2713448]
29. Karanikas G, Beheshti M. (1)(1)C-acetate PET/CT imaging: physiologic uptake, variants, and pitfalls. PET clinics. 2014; 9:339–44. [PubMed: 25030397]
30. Louis P, Hold GL, Flint HJ. The gut microbiota, bacterial metabolites and colorectal cancer. Nature reviews Microbiology. 2014; 12:661–72. [PubMed: 25198138]
31. Oyajobi BO, Goins B, Gupta A, Zavaleta C, Grubbs B, Wideman C, et al. Imaging tumor burden by [F-18]FDG-PET and osteoblast activity by [Tc-99m]MDP-SPECT/CT in the 5TGM1 mouse model of myeloma bone disease. J Bone Miner Res. 2005; 20:S212-S.
32. Amend SR, Wilson WC, Chu L, Lu L, Liu P, Serie D, et al. Whole Genome Sequence of Multiple Myeloma-Prone C57BL/KaLwRij Mouse Strain Suggests the Origin of Disease Involves Multiple Cell Types. PloS one. 2015; 10:e0127828. [PubMed: 26020268]

33. Soodgupta D, Pan D, Cui G, Senpan A, Yang X, Lu L, et al. Small Molecule MYC Inhibitor Conjugated to Integrin-Targeted Nanoparticles Extends Survival in a Mouse Model of Disseminated Multiple Myeloma. Molecular cancer therapeutics. 2015; 14:1286–94. [PubMed: 25824336]
34. Soodgupta D, Hurchla MA, Jiang M, Zheleznyak A, Weilbaecher KN, Anderson CJ, et al. Very late antigen-4 (alpha(4)beta(1) Integrin) targeted PET imaging of multiple myeloma. PloS one. 2013; 8:e55841. [PubMed: 23409060]
35. Oyajobi BO, Munoz S, Kakonen R, Williams PJ, Gupta A, Wideman CL, et al. Detection of myeloma in skeleton of mice by whole-body optical fluorescence imaging. Molecular cancer therapeutics. 2007; 6:1701–8. [PubMed: 17541032]
36. Vieira P, Rajewsky K. The half-lives of serum immunoglobulins in adult mice. European journal of immunology. 1988; 18:313–6. [PubMed: 3350037]
37. Sanchez E, Li M, Kitto A, Li J, Wang CS, Kirk DT, et al. Serum B-cell maturation antigen is elevated in multiple myeloma and correlates with disease status and survival. British journal of haematology. 2012; 158:727–38. [PubMed: 22804669]
38. Terpos E, Dimopoulos MA, Moulopoulos LA. The Role of Imaging in the Treatment of Patients With Multiple Myeloma in 2016. American Society of Clinical Oncology educational book/ASCO American Society of Clinical Oncology Meeting. 2016; 35:e407–17.
39. Zamagni E, Patriarca F, Nanni C, Zannetti B, Englaro E, Pezzi A, et al. Prognostic relevance of 18-F FDG PET/CT in newly diagnosed multiple myeloma patients treated with up-front autologous transplantation. Blood. 2011; 118:5989–95. [PubMed: 21900189]
40. Vij R, Fowler KJ, Shokeen M. New Approaches to Molecular Imaging of Multiple Myeloma. Journal of nuclear medicine: official publication, Society of Nuclear Medicine. 2016; 57:1–4.
41. van Lammeren-Venema D, Regelink JC, Riphagen II, Zweegman S, Hoekstra OS, Zijlstra JM. (1)(8)F-fluoro-deoxyglucose positron emission tomography in assessment of myeloma-related bone disease: a systematic review. Cancer. 2012; 118:1971–81. [PubMed: 21887677]
42. Ho CL, Chen S, Leung YL, Cheng T, Wong KN, Cheung SK, et al. 11C-acetate PET/CT for metabolic characterization of multiple myeloma: a comparative study with 18F-FDG PET/CT. Journal of nuclear medicine: official publication, Society of Nuclear Medicine. 2014; 55:749–52.
43. Lin C, Ho CL, Ng SH, Wang PN, Huang Y, Lin YC, et al. (11)C-acetate as a new biomarker for PET/CT in patients with multiple myeloma: initial staging and postinduction response assessment. European journal of nuclear medicine and molecular imaging. 2014; 41:41–9. [PubMed: 24129710]
44. Yu EY, Muzi M, Hackenbracht JA, Rezvani BB, Link JM, Montgomery RB, et al. C11-acetate and F-18 FDG PET for men with prostate cancer bone metastases: relative findings and response to therapy. Clinical nuclear medicine. 2011; 36:192–8. [PubMed: 21285676]
45. Hanahan D, Weinberg RA. Hallmarks of cancer: the next generation. Cell. 2011; 144:646–74. [PubMed: 21376230]
46. Vriezen N, van Dijken JP. Fluxes and enzyme activities in central metabolism of myeloma cells grown in chemostat culture. Biotechnology and bioengineering. 1998; 59:28–39. [PubMed: 10099311]
47. Fagone P, Sriburi R, Ward-Chapman C, Frank M, Wang J, Gunter C, et al. Phospholipid biosynthesis program underlying membrane expansion during B-lymphocyte differentiation. The Journal of biological chemistry. 2007; 282:7591–605. [PubMed: 17213195]
48. McGehee AM, Dougan SK, Klemm EJ, Shui G, Park B, Kim YM, et al. XBP-1-deficient plasmablasts show normal protein folding but altered glycosylation and lipid synthesis. Journal of immunology. 2009; 183:3690–9.
49. Tirado-Velez JM, Joumady I, Saez-Benito A, Cozar-Castellano I, Perdomo G. Inhibition of fatty acid metabolism reduces human myeloma cells proliferation. PloS one. 2012; 7:e46484. [PubMed: 23029529]
50. Yoshii Y, Furukawa T, Oyama N, Hasegawa Y, Kiyono Y, Nishii R, et al. Fatty acid synthase is a key target in multiple essential tumor functions of prostate cancer: uptake of radiolabeled acetate as a predictor of the targeted therapy outcome. PloS one. 2013; 8:e64570. [PubMed: 23741342]

51. Haseebuddin M, Dehdashti F, Siegel BA, Liu J, Roth EB, Nepple KG, et al. 11C-acetate PET/CT before radical prostatectomy: nodal staging and treatment failure prediction. Journal of nuclear medicine: official publication, Society of Nuclear Medicine. 2013; 54:699–706.

STATEMENT OF TRANSLATIONAL RELEVANCE

Metabolic imaging is a key tool in the diagnosis, management and evaluation of treatment response in a variety of cancer types. Herein we provide proof-of-concept evidence for the use of ^{11}C-acetate-PET metabolic imaging of multiple myeloma (MM) in preclinical models to assess tumor burden and early response to therapy. The molecular basis of tracer uptake was elucidated *via in vitro* acetate metabolism by metabolite fate tracking and pharmacological modulation of its pathways. We demonstrated that myeloma cells are dependent on monocarboxylic acid anabolic metabolism, to which acetate contributes, and hence could serve as a therapeutic target. This translates into a direct correlation between viable MM cells and acetate uptake at tumor sites, and a rapid decrease in acetate *in vivo* uptake upon administration of anti-myeloma treatments. In summary, our results support the rationale for prospective clinical studies using ^{11}C-acetate for staging and early assessment of treatment response in MM patients.

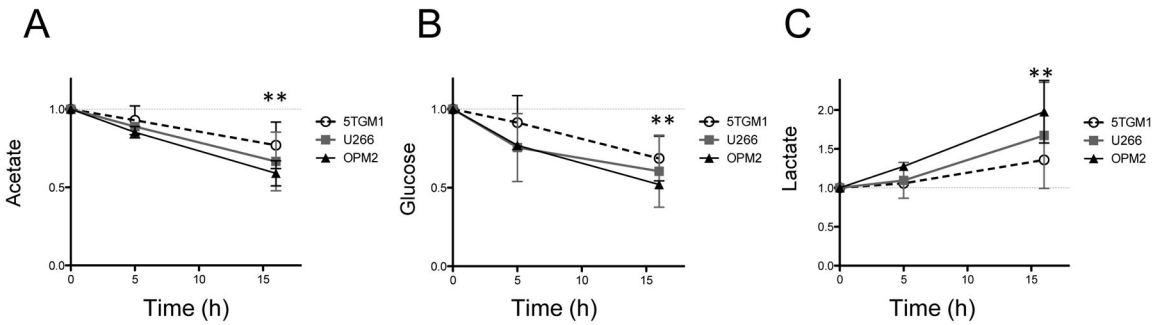

D

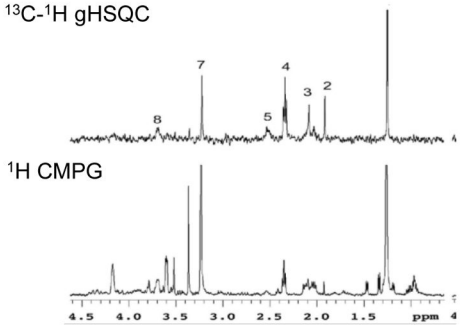

Peak #	Chemical Shift	Group	Putative Assignment
1	1.24	$-C(CH_3)_3$	t-butanol (internal standard)
2	1.91	$-C(O)CH_3$	Acetate
3	2.06-2.08	$-NC(O)CH_3$	3-glutamate
4	2.34-2.38 ppm	$-CH_2-$	4-glutamate, Oxalacetic acid
5	2.53	$-CH_2-$	GSH
6	2.66		
7	3.22 (3.21-3.23) ppm	$-N(CH_3)_3$	Phosphocholine/Choline
8	3.71		2-glutamine

E

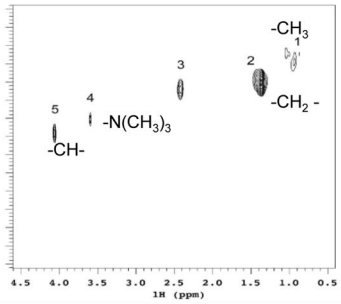

Peak #	^{1}H ppm	^{13}C ppm	Group	Putative Assignment
1	0.9-0.95	19.6-19.7	$R-CH_3$	Fatty Acid chain
2	1.36	30.5-30.6	$-(CH_2)_n-$	Fatty Acid chain
3	2.3-2.5	34.2-34.4		Hydoxybutyrate
4	3.2-3.7	50.5-50.1	$-N(CH_3)_3-$	Phosphocholine group
5	4.0-4.1	58-59	-CH-	Glycerol backbone

Figure 1. ^{13}C-edited ^{1}H-NMR shows metabolism of acetate by MMC and uptake of acetate from the extracellular environment

A) ^{1}H NMR (CPMG) analysis of acetate (1.91 ppm) in the conditioned media from MMC lines 5TGM1, U266, and OPM2, incubated for different times with 10mM acetate. B) Analysis of glucose (5.24 ppm), C) Analysis of Lactate (1.31–1.32 ppm). Acetate, glucose and lactate values are normalized by alanine (3-position at 1.5 ppm) and time 0. Average (dots) and standard deviation (error bars) of 2–3 biological replicates are shown per time-point per cell line, ** $p<0.01$ by two-way ANOVA.

D) Intracellular acetate metabolism assessment by metabolite fate tracking by NMR showing the ^{13}C-^{1}H gHSQC (gradient Heteronuclear Single Quantum Coherence, top)

and ^{1}H CPMG spectra from the same cellular extract of U266 human MMC incubated for 16h with 10mM ^{13}C-acetate. Peak assignments (by number) and ^{1}H chemical shift in the table on the right.

E) 2D ^{1}H-^{13}C HSQC of U266 chloroform extraction (membranes) after 70h incubation with 10mM ^{13}C-acetate (chemical shifts and metabolite assignment in the table on the right).

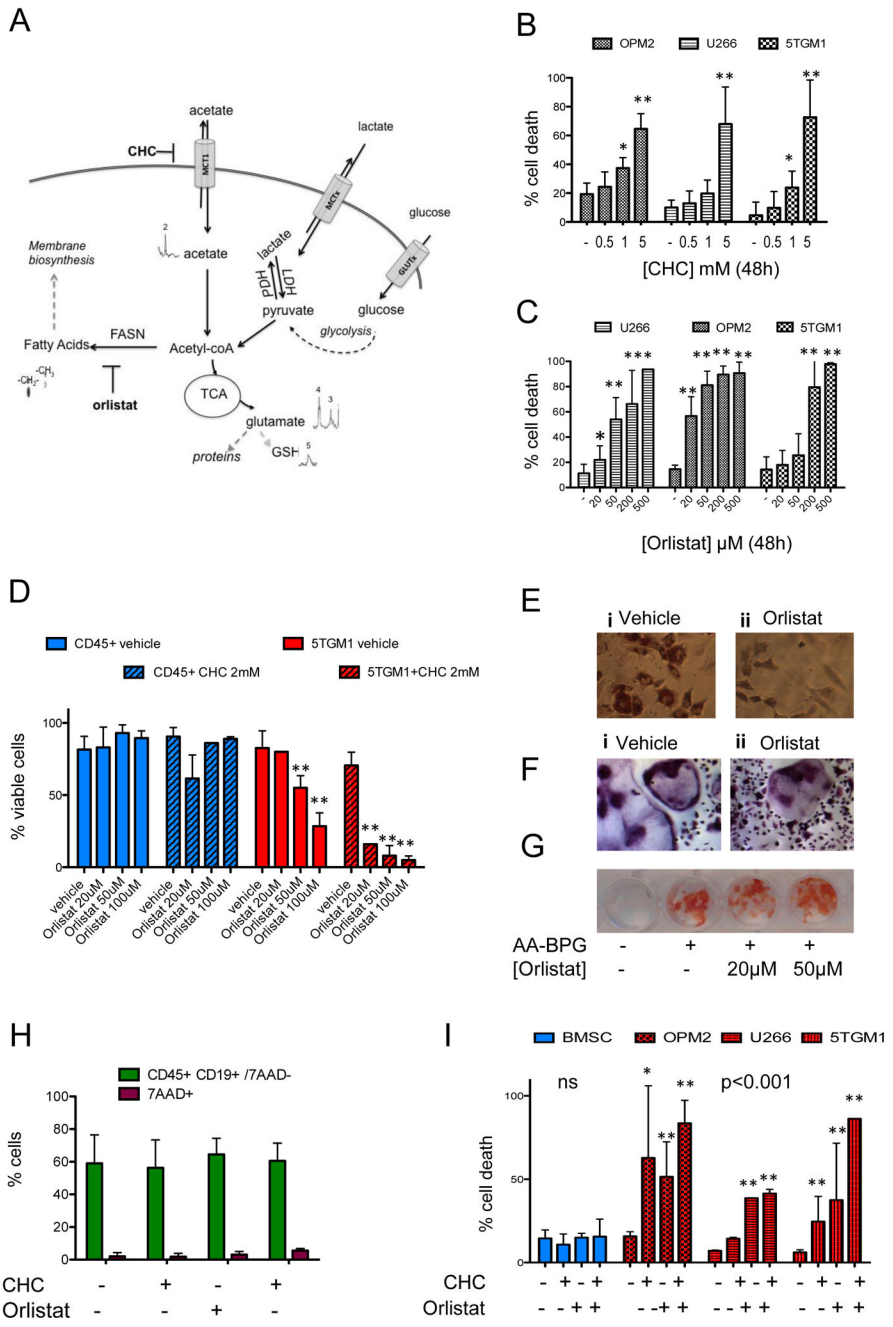

Figure 2. Pharmacological modulation of acetate metabolism leads to toxicity in MMC while sparing the surrounding BM resident cells

A) Working model. Labeled acetate is imported from the extracellular environment through monocarboxylate transporters such as MCT1, is found inside cells (^{13}C-NMR), where it may be activated to Acetyl-CoA. This can rapidly enter the TCA cycle and be transformed into glutamate (peaks 3 and 4) and participate in multiple reactions, including being incorporated into glutathione (GSH peak 5). Acetyl-CoA can also be a substrate for *de-novo* biosynthesis of fatty acids through the activity of fatty acid synthase (FASN), providing building blocks for cell membranes. CHC is a known inhibitor of MCT1, orlistat of FASN. Other

monocarboxylic acids that can be involved in the same reactions include lactate, which is produced and released in the media by MMC and also pyruvate, as end-product of glycolysis. B) Treatment with α-cyano-4-hydroxycinnamic acid (CHC) induces MM cell death. Propidium Iodide staining and flow cytometry upon 48h incubation with 0–5mM CHC of OPM2, U266, or 5TGM1 cells (mean and standard deviation of 2–3 biological replicates per cell line, two-way ANOVA $p<0.01$ dose, cell line ns). C) Treatment with FASN inhibitor orlistat induces cell death in MMC lines. Propidium Iodide positive cells percentage by flow cytometry (mean and standard deviation of 2 to 8 biological replicates) upon treatment with 20–500μM orlistat in U266, OPM2, and 5TGM1 MMC for 48h (two-way ANOVA $p<0.01$). D) Cell viability by trypan blue staining, relative to untreated control, upon 48h treatment with orlistat (20–100 μM) plus vehicle (DMSO, open bars) or CHC 2mM (dashed bars) in primary mouse CD45+ spleen cells (blue bars) or 5TGM1 (red bars), showing sensitivity to single-agent and combined treatment in 5TGM1 (orlistat <0.01, interaction with CHC <0.05 by two-way ANOVA). E) Oil-red-O staining and hematoxylin counter-staining of ST2 cells induced to differentiate with adipogenic media (insulin, indomethacin, dexamethasone) for 14 days in the absence (left, i.) or presence (right, ii.) of 100 μM orlistat shows that long-term FASN inhibition prevents adipogenic differentiation but does not induce death of mesenchymal cells. F) Tartrate-resistant acid phosphatase (TRAP) staining of mouse bone marrow monocytes induced to differentiate to osteoclasts with M-CSF and RANKL shows formation of TRAP-positive multinucleated cells in the absence (left, i.) or presence (right, ii.) of 50 μM orlistat for 6 days. G) Alizarin-Red staining of mouse bone marrow stromal cells (BMSC) after standard culture (−) or osteogenic differentiation (+) with β-glycerophosphate (BPG) and ascorbic acid (AA) for 21 days shows mineralized matrix formation in the absence (−) or presence of orlistat (20 or 50 μM). H) Flow cytometry of mouse splenocytes treated for 48h with CHC (2mM) and/or Orlistat (100 μM) showing 7AAD+ dead cells (purple bars) vs. CD45+ CD19+ 7AA− B cells (ns). I) Cell death as % PI positive cells upon treatment with CHC and orlistat in primary BMSC (blue) vs. OPM2, U266 or 5TGM1 MMC (red) upon treatment with CHC, alone or in combination with Orlistat for 48h. Average of biological replicates, standard deviations as error bars, * $p<0.05$, ** $p<0.001$ (one-way ANOVA) relative to control.

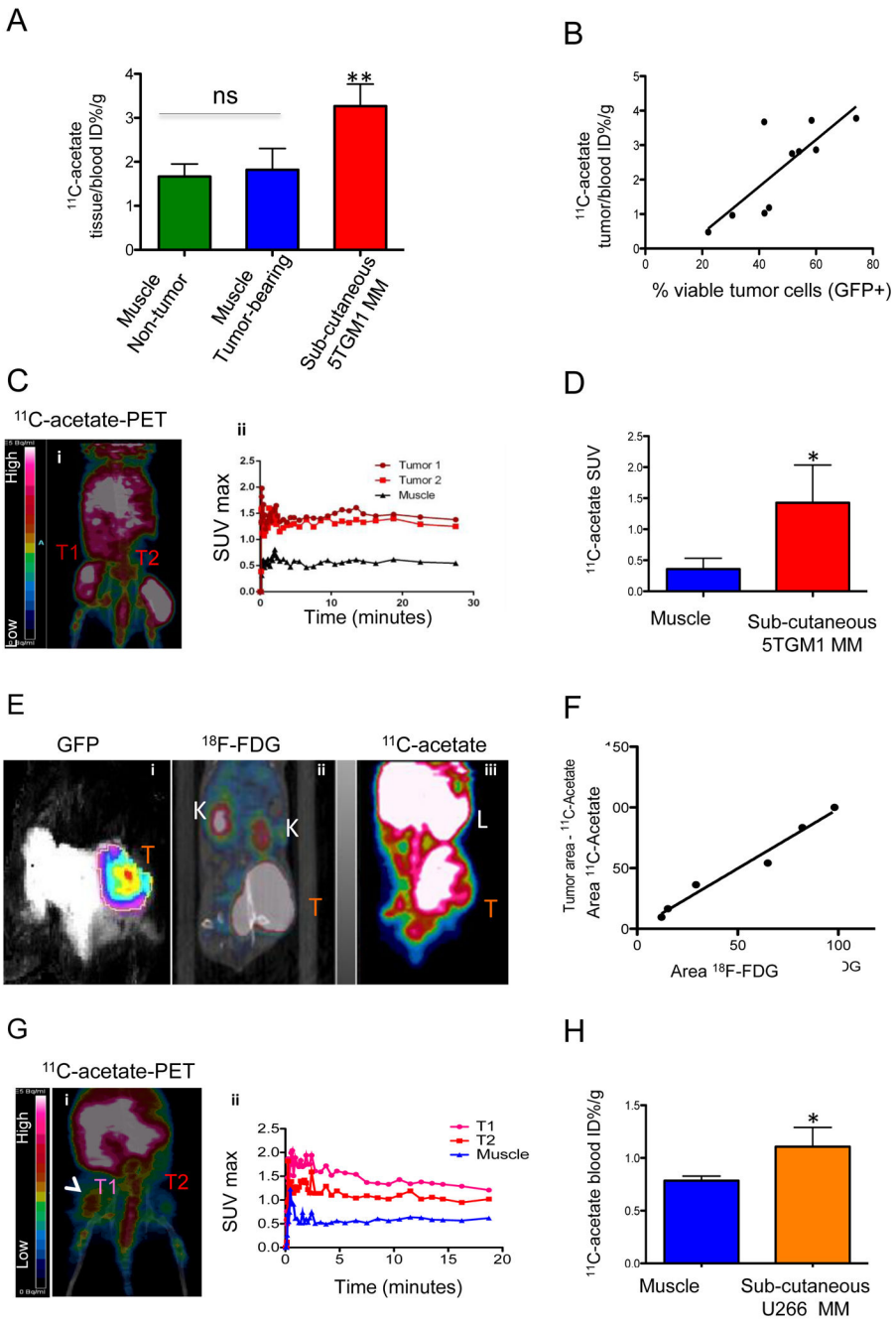

Figure 3. ^{11}C-acetate uptake in MM subcutaneous plasma cell tumors (PCT)

A) Bio-distribution of ^{11}C-acetate at 1 hour post injection in KaLwRij mice showing uptake in the muscle of non tumor-bearing (n=2 green) or tumor-bearing (n=3 blue) vs. subcutaneous 5TGM1-tumors (n=6 red). ** p<0.01 by ANOVA with Tuckey's multiple-comparison post-hoc test. B) Correlation between ^{11}C-acetate bio-distribution and number of viable tumor cells (GFP+ PI−) in 5TGM1 subcutaneous PCT in KaLwRij mice Pearson's r=0.8, p<0.01). C) ^{11}C-acetate PET imaging (i) of a female NSG mouse at day 30 after bilateral inoculation with 5TGM1-GFP cells (1×106 in matrigel) and time-activity curves

(TAC, ii) from tumors and muscle regions of interest (ROI). Mice were injected with 20 MBq ^{11}C-acetate and scanned by dynamic PET for 0–30 minutes. D) Maximum standardized uptake value (SUV_{max}) in muscle ROI vs. subcutaneous 5TGM1 PCT in KaLwRij mice imaged with ^{11}C-acetate PET (n=5).

E) (i) KaLwRij muose bearing a subcutaneous 5TGM1 PCT imaged by optical imaging (480/535 nm for GFP, overlay of intensity pseudocolor on bright field), (ii), FDG-PET/CT, and ^{11}C-acetate PET.

F) Correlation between ROI measured in small animal PET using FDG (x axis) or ^{11}C-acetate (y axis) in KaLwRij mice with subcutaneous 5TGM1 PCT; r=0.98, p<0.01 G) Small animal ^{11}C-acetate PET/CT image (i) with TAC (dynamic 0–20 minutes) (**ii**) for muscle (blue) and tumors (T1/T2) in U266 human MMC bilateral xenograft (3.5×107 cells in matrigel, 1200 mm^3 T1 and 150 mm^3 T2) in a NSG female mouse. H) Tissue bio-distribution of ^{11}C-acetate 1 hour after injection in NSG mice (n=3) with bilateral U266 subcutaneous tumors (n=6), showing ratio of tissue to blood %ID/g. * p<0.05 by T-test. T=Tumor, K=kidneys, L= liver; ns=not-significant, * p<0.05, ** p<0.01

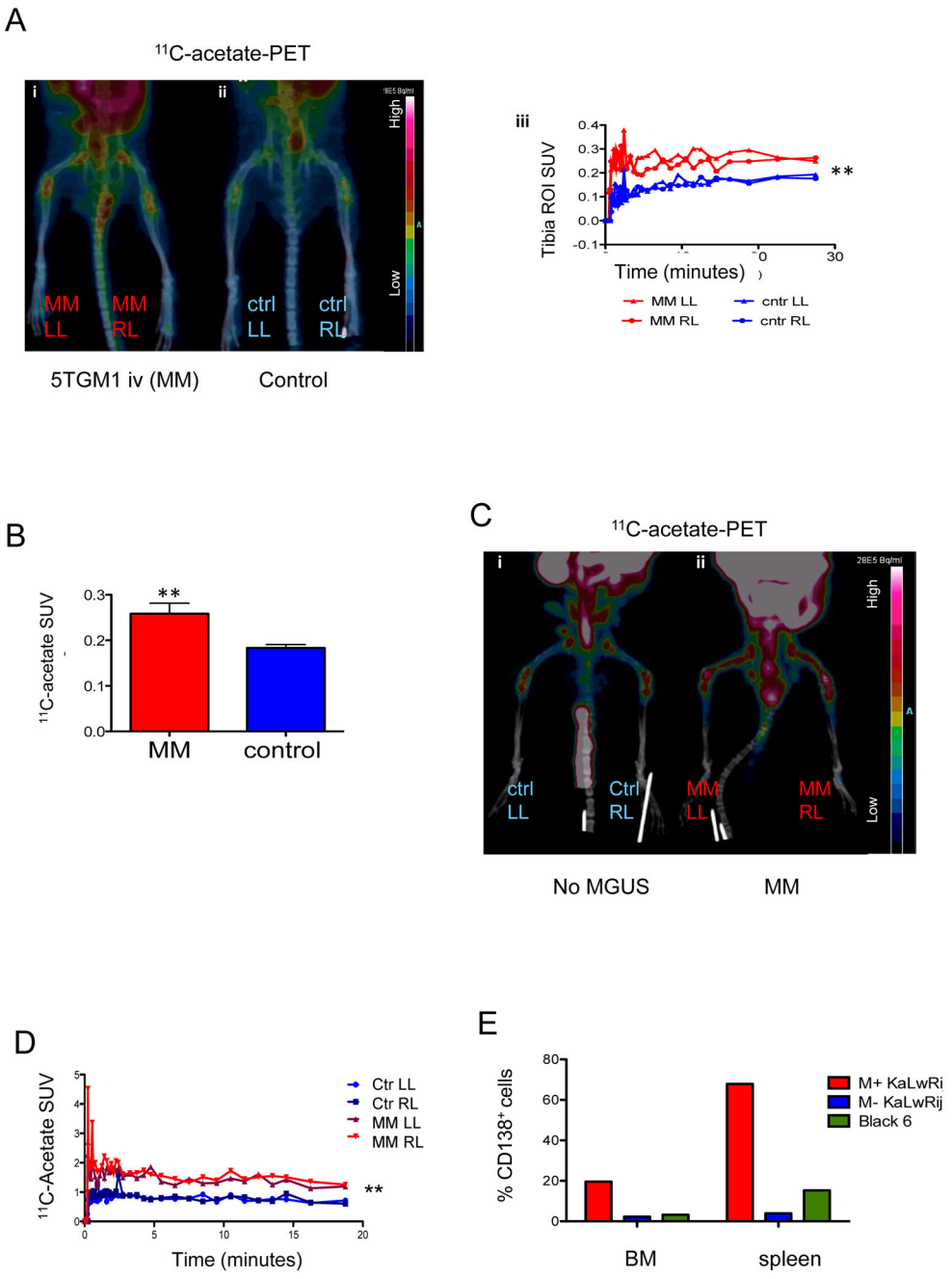

Figure 4. ^{11}C-acetate uptake in bone-localized MM

A) (i.) ^{11}C-acetate PET/CT image of a KaLwRij mouse bearing i.v. 5TGM1 MM cells (21 days post tumor inoculation); (ii.) ^{11}C-acetate PET/CT image of a control KaLwRij mouse (iii) TAC of MM (red) and control (blue) bones. ROIs were defined around the tibial diaphysis. ** $p<0.01$ by ANOVA.

B) SUVs from the tibial ROI of 5TGM1 iv injected KaLwRij mice vs. controls (n=4).

C) ^{11}C-acetate PET/CT image of1 year old KaLwRij mice, without (**i.**, control) or with sustained M-component at the SPEP (**ii.** Right, MM). D) TAC for the tibial diaphysis ROI

shows significantly higher uptake in the mouse with gammopathy (MM). E) Flow cytometry analysis of bone marrow and spleen homogenate upon staining with anti-CD138 reveals pathologic elevation of plasma cell counts ($CD138^+$ cells) in the spleen and bone marrow in the aged mouse with gammopathy (red), relative to the SPEP-negative KaLwRij (blue) or C57/BL6 (green) age-matched controls, consistent with MM. *$p<0.05$, ** $p<0.01$

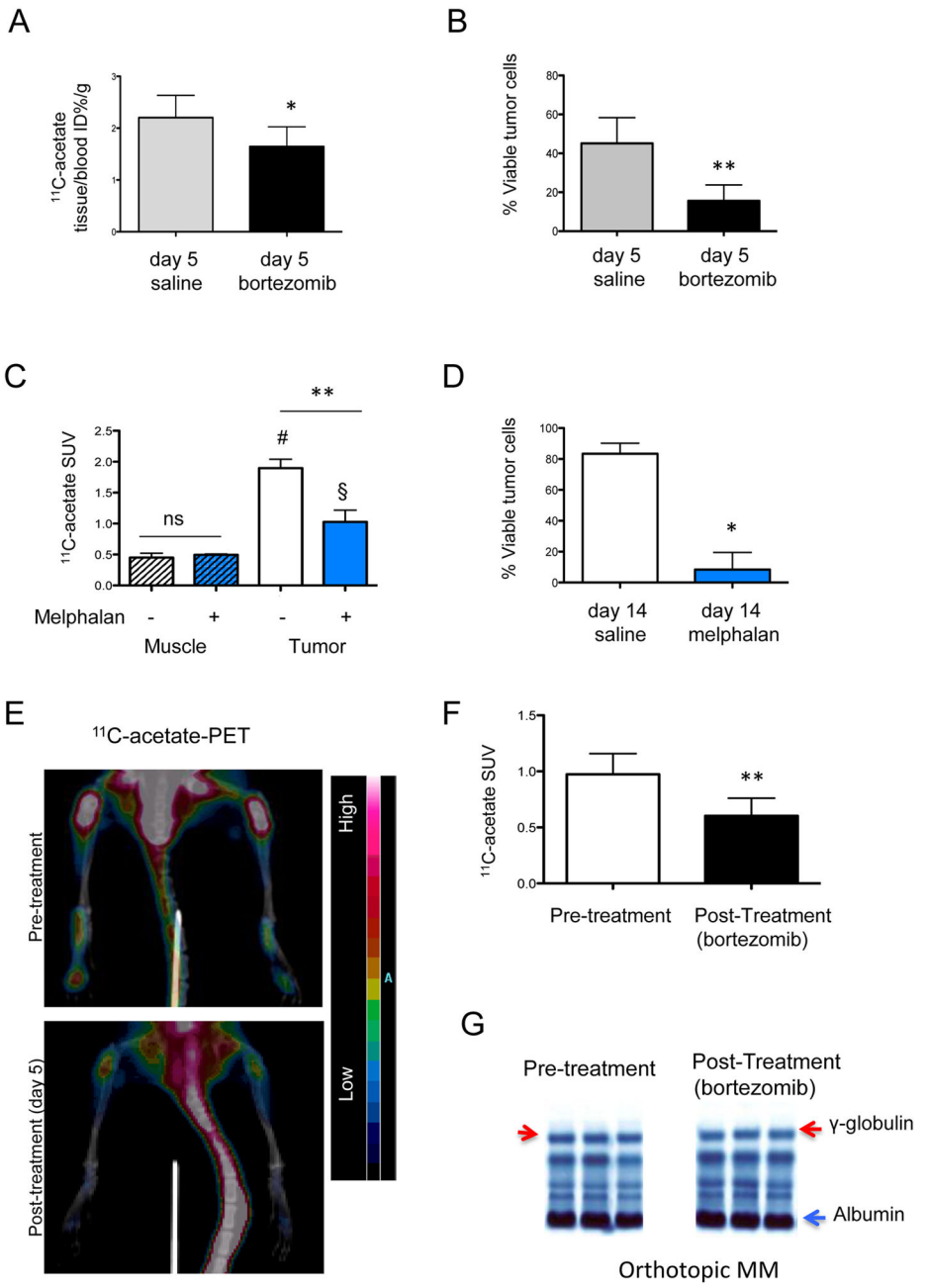

Figure 5. ^{11}C-acetate uptake reports on response to bortezomib

A–B) Tissue bio-distribution (A) 1h post ^{11}C-acetate injection and ex-vivo tumor cell viability (GFP+ PI− cells, B) in KaLwRij mice with subcutaneous 5TGM1 tumors, on day 5 of treatment with saline (gray) or bortezomib (day1–day 4, 1mg/kg) C–D) ^{11}C-acetate PET tumor and muscle SUV (C) and *ex-vivo* tumor viability (GFP+ PI− cells, D) in KaLwRij mice with subcutaneous 5TGM1 tumors treated for two weeks with vehicle (open bars) vs. melphalan (blue bars) (n=2/group) C-acetateANOVA and Tukey's post-hoc test $p<0.01$ for treated vs. untreated tumors (**), $p<0.01$ for muscle vs. untreated (#) and $p<0.05$ vs. remaining treated tumor (§).C-acetateE) ^{11}C-acetate PET/CT of a representative orthotopic

5TGM1 MM-bearing KaLwRij mouse before (top) and a day after (bottom, day 5) treatment with bortezomib, showing decreased bone uptake (see heat map scale) in the post-treatment scan on day 5 since the beginning of treatment with bortezomib. F) SUVs from the tibial ROI before and 5 days after treatment with bortezomib of 5TGM1 MM-bearing KaLwRij mice (n=3 mice, 6 total ROIs). G) Serum Protein Electrophoresis (SPEP) of three 5TGM1 MM-bearing mice prior to (left) and after (right) 5 days of treatment with bortezomib, showing the lack of increase, but presence of an identifiable monoclonal band in the γ-globulin region (red arrow). *$p<0.05$, ** $p<0.01$